Monthly Notices of the ROYAL ASTRONOMICAL SOCIETY

MNRAS **449,** 1782–1796 (2015) doi:10.1093/mnras/stv369

The JCMT Gould Belt Survey: properties of star-forming filaments in Orion A North

C. J. Salji,[1,2]★ J. S. Richer,[1,2] J. V. Buckle,[1,2] J. Di Francesco,[3,4] J. Hatchell,[5] M. Hogerheijde,[6] D. Johnstone,[3,4,7] H. Kirk,[3] D. Ward-Thompson[8] and on behalf of the JCMT GBS Consortium†

[1]*Astrophysics Group, Cavendish Laboratory, J J Thomson Avenue, Cambridge CB3 0HE, UK*
[2]*Kavli Institute for Cosmology, Institute of Astronomy, University of Cambridge, Madingley Road, Cambridge CB3 0HA, UK*
[3]*NRC Herzberg Astronomy and Astrophysics, 5071 West Saanich Rd, Victoria, BC V9E 2E7, Canada*
[4]*Department of Physics and Astronomy, University of Victoria, Victoria, BC V8P 1A1, Canada*
[5]*Physics and Astronomy, University of Exeter, Stocker Road, Exeter EX4 4QL, UK*
[6]*Leiden Observatory, Leiden University, PO Box 9513, NL-2300 RA Leiden, the Netherlands*
[7]*Joint Astronomy Centre, 660 N. A'ohōkū Place, University Park, Hilo, Hawaii 96720, USA*
[8]*Jeremiah Horrocks Institute, University of Central Lancashire, Preston, Lancashire PR1 2HE, UK*

Accepted 2015 February 19. Received 2015 January 26; in original form 2014 July 22

ABSTRACT

We develop and apply a Hessian-based filament detection algorithm to submillimetre continuum observations of Orion A North. The resultant filament radial density profiles are fitted with beam-convolved line-of-sight Plummer-profiles using Markov chain Monte Carlo techniques. The posterior distribution of the radial decay parameter demonstrates that the majority of filaments exhibit $p = 1.5$–3, with a mode at $p = 2.2$, suggesting deviation from the Ostriker $p = 4$ isothermal, equilibrium, self-gravitating cylinder. The spatial distribution of young stellar objects relative to the high column density filaments is investigated, yielding a lower limit on the star-forming age of the integral-shaped filament ∼1.4 Myr. Additionally, inferred lifetimes of filaments are examined which suggest long-term filament accretion, varying rates of star formation, or both. Theoretical filament stability measures are determined with the aid of HARP $C^{18}O$ $J = 3$–2 observations and indicate that the majority of filaments are gravitationally subcritical, despite the presence of young protostars. The results from this investigation are consistent with the one-dimensional accretion flow filament model recently observed in numerical simulations.

Key words: stars: formation – stars: protostars – ISM: structure – submillimetre: ISM.

1 INTRODUCTION

The process of star formation is strongly associated with molecular clouds and their structural overdensities (McKee & Ostriker 2007; Lombardi, Alves & Lada 2010). Filamentary structure in particular has become an area of great interest as modern submillimetre telescopes have revealed a plethora of complex structure associated with cold cores and young stellar objects (YSOs; André et al. 2010; Hill et al. 2011; Buckle et al. 2012). In support of this, hydrodynamical simulations predict the existence of high-density filaments that flow into star-forming clusters (Gómez & Vázquez-Semadeni 2014), while analytical models suggest that cylindrical geometries favour gravitational collapse over alternative geometries (Pon, Johnstone & Heitsch 2011). Previous studies of filamentary structure in Aquila, Polaris and IC 5146 using data from the *Herschel* Space Observatory have yielded results suggestive of a characteristic filament width of ∼0.1 pc (Arzoumanian et al. 2011) and a radial fall-off parameter $p \sim 2$ (see equation 4) consistent with the presence of helical magnetic fields (Fiege & Pudritz 2000) rather than a static isothermal self-gravitating cylinder (Ostriker 1964). The accurate determination of such quantities depends heavily upon spatial resolution as filaments at a distance of ∼400 pc are

★E-mail: cs673@cam.ac.uk
†The full members of the JCMT Gould Belt Survey Consortium are P. Bastien, D. Berry, S. Beaulieu, J. Buckle, H. Butner, A. Duarte-Cabral, A. Chrysostomou, S. Coude, M. Currie, C. J. Davis, E. Drabek-Maunder, J. Di Francesco, M. Fich, J. Fiege, L. M. Fissel, P. Friberg, R. Friesen, G. Fuller, S. Graves, J. Greaves, J. Gregson, J. Hatchell, M. Hogerheijde, W. Holland, T. Jenness, D. Johnstone, G. Joncas, J.M. Kirk, H. Kirk, L.B.G. Knee, S. Mairs, K. Marsh, B.C. Matthews, J.C. Mottram, C. Quinn, J. Rawlings, J. Richer, D. Robertson, E. Rosolowsky, D. Rumble, S. Sadavoy, C. Salji, G. Schieven, N. Tothill, H. Thomas, S. Viti, D. Ward-Thompson, G.J. White, C. Wilson, J. Wouterloot, J. Yates, and M. Zhu.

barely resolved using the *Herschel* instruments (Juvela, Malinen & Lunttila 2012). The use of larger ground-based telescopes such as JCMT with SCUBA-2 (Holland et al. 2013) can exceed the resolving power of *Herschel* instruments by >2.5, potentially allowing for more precise determination of filament properties. Alternatively, this capability may allow for probing the properties of filaments at greater distances and in differing environments – providing data that can validate the hypothesis of characteristic filament widths if applied to large quantities of observational data. To derive statistically sound filament properties, quantities from large samples of observational data must be extracted in an automated and unbiased manner. In this study, we apply for the first time, a multiscale Hessian-based filament enhancement and extraction technique to derive filament properties using column density and temperature maps generated from SCUBA-2 450 and 850 μm observations of Orion A North. This region (also known as the 'integral-shaped filament' (ISF)) is one of the most active and well-studied sites of star formation near to the Sun (Johnstone & Bally 1999). Distance estimates of Orion A vary considerably but the vast majority lie in the range of 400–500 pc (Muench et al. 2008; Schlafly et al. 2014). Consequently, we adopt a distance of 450 pc – comparable to the IC 5146 filament (∼460 pc) studied in Arzoumanian et al. (2011). This investigation provides additional, independently obtained filament data from a more distant molecular cloud, with differing physical conditions, at super-*Herschel* resolution.

2 DATA REDUCTION AND FLUX CALIBRATION

The observations were obtained using the SCUBA-2 instrument, mounted on the James Clerk Maxwell Telescope (JCMT) near the peak of Mauna Kea, Hawaii. SCUBA-2 offers resolutions of ∼8 and 13 arcsec FWHM (full width at half-maximum) at 450 and 850 μm (Dempsey et al. 2013). A total of 17, ∼40 min observations, each using the 1800 arcsec-wide SCUBA-2 'pong' mapping method (Kackley et al. 2010) were taken between late 2011 October and 2013 September as part of the JCMT Gould Belt Survey (GBS; Ward-Thompson et al. 2007a) with Program ID MJLSG31. Observations used in the final mosaic were a blend of science verification and legacy survey data, taken in band 1 and 2 weather ($\tau_{225} < 0.08$).

The bolometer time series data were reduced using the SCUBA-2 iterative map maker (Chapin et al. 2013) with the JCMT GBS Internal Release 1 configuration file. A 600 arcsec spatial filter was employed to aid in the removal of sky signal at both 450 and 850 μm. The 17 maps were reduced individually using autogenerated 'masks' which identify emission-free regions to assist convergence of the iterative map maker. Additionally, decontamination of the 850 μm dust continuum from the ^{12}CO $J = 3$–2 emission line was achieved according to the process and data outlined in Salji, Richer & Buckle (2015). These individually reduced maps are then mosaicked to produce a higher sensitivity map to better estimate the emission-free regions and further aid the iterative map maker in the final reduction. Flux conversion factors (FCFs) of 468± 59 and 532± 20 Jy beam^{-1} pW^{-1}, at 450 and 850 μm, respectively, were derived from the sample of calibration measurements corresponding to the nights of observation. These nightly 450 and 850 μm FCF measurements are positively correlated, leading to an FCF ratio which varies by ∼12 per cent. The uncertainty in this FCF ratio far exceeds the thermal noise of the bolometers (in regions with signal) and may be considered the limiting factor when deriving temperature estimates using SCUBA-2 (see Section 3). The 'pong' mapping method produces non-uniform sensitivity; however, the standard deviation of the mean of bolometer signals within each pixel provides noise estimates of ∼40 and 7 mJy beam^{-1} at 450 and 850 μm, respectively.

3 COLUMN DENSITY AND TEMPERATURE MAP GENERATION

This process is discussed only briefly here, for greater depth of discussion see Salji et al. (2015). For the temperature and column density determination, we assume the dust emission to be optically thin ($\tau_\nu \ll 1$), fix the dust emissivity index at $\beta = 2$ and the dust opacity at $\kappa_{\nu_0} = 0.1$ cm^2 g^{-1} where ν_0=1000 GHz in accordance with Arzoumanian et al. (2011). Thus, the expected intensity of dust emission is given by

$$I_\nu = \kappa_{\nu_0} \left(\frac{\nu}{\nu_0}\right)^\beta \Sigma\, B_\nu(T), \tag{1}$$

where Σ is the dust column density and $B_\nu(T)$ is the Planck function. The ratio of intensities at 450 and 850 μm is independent of column density and directly relates to the dust temperature via the implicit equation:

$$\frac{I_{850}}{I_{450}} = \left(\frac{\nu_{850}}{\nu_{450}}\right)^{3+\beta} \left(\frac{\exp\frac{h\nu_{450}}{kT} - 1}{\exp\frac{h\nu_{850}}{kT} - 1}\right). \tag{2}$$

Accurate evaluation of this ratio and ultimately the temperature and column density values require beam matching of the two intensity measurements. This process is achieved through the generation and application of a convolution kernel which solves:

$$K_{450\Rightarrow850} = \mathrm{FT}^{-1}\left[\frac{\mathrm{FT}(B_{850})}{\mathrm{FT}(B_{450})}\right], \tag{3}$$

where $K_{450\Rightarrow850}$, B_{850} and B_{450} are the convolution kernel and the SCUBA-2 850 and 450 μm beam models, respectively. The derivation, application and accuracy of the convolution kernel are described in Salji et al. (2015). The temperature map was generated via a look up table to solve the implicit equation (2). At temperatures $> \frac{h\nu}{k_B}$ the measured flux ratio provides only weak constraints on dust temperature. At 450 μm $\frac{h\nu}{k_B} \sim 32$ K and as a result, we adopt 50 K as the upper limit for the temperature lookup. Consequently, all regions with temperature values exceeding 50 K in Fig. 1 are blank (white). The final column density and temperature maps were produced by first deriving the temperature from the 450 to 850 μm intensity ratio as in equation (2). In addition to the single T values, the most extreme values (low and high) were derived using the 1σ uncertainty of the FCF ratio measurements – 12 per cent. These T values propagate through to the column density estimate via equation (1), resulting in the final temperature and column density maps (see Figs 1 and 4) with associated uncertainty.

4 VELOCITY INFORMATION FROM MOLECULAR TRACERS

In addition to the dust continuum measurements mentioned above, we also examine supporting data in the form of C^{18}O $J = 3$–2 observations of Orion A North observed as part of the JCMT GBS using HARP (Buckle et al. 2012). These observations provide key information regarding the kinetic energy of the filaments which provides resistance to the gravitational collapse and ultimately the formation of stars. The C^{18}O line profiles were fitted with a skew-Gaussian model – in effect, a Gaussian with the potential for differing values of σ either side of the central peak (see Fig. 2). This

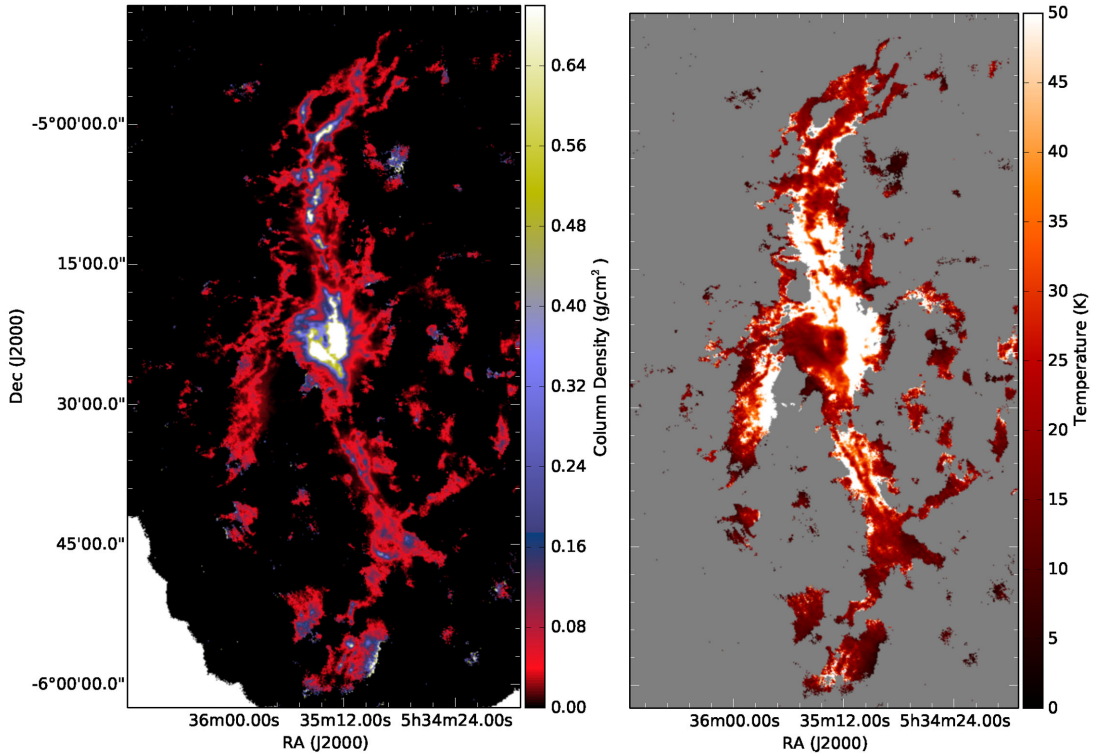

Figure 1. Column density (left) and temperature (right) maps of Orion A North. Regions where the signal-to-noise ratio of the 450 and 850 μm intensities drops below 5σ are coloured grey. The maximum, mean, median and standard deviation of the column density values are (112, 0.13, 0.04, 1.24) g cm^{-2}. The maximum, mean, median and standard deviation of the temperature values are (50.0, 25.5, 20.1, 14.3) K.

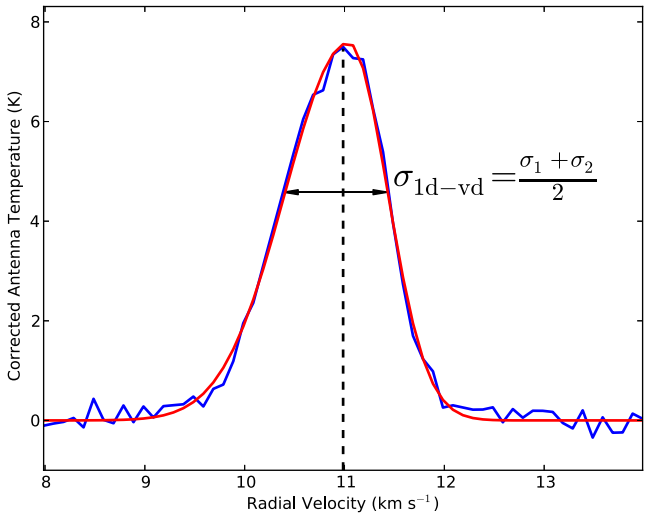

Figure 2. C^{18}O, $J = 3$–2 line emission (blue) and skew-Gaussian fit (red) at a pixel within Filament 26. The variables σ_1 and σ_2 are the Gaussian standard deviations either side of the central peak which are averaged to provide a more accurate estimate of the velocity dispersion when the emission line profile is asymmetric.

allows for more accurate fitting to asymmetric line profiles such as those exhibited by protostellar outflows which are thought to contribute significantly to the turbulent support of filaments (Li & Nakamura 2006).

It should be noted that while there is obvious scope for a more detailed study of velocity-resolved filaments, especially in three-dimensions, we restrict ourselves in this study to using the C^{18}O emission to investigate solely the criticality of filaments in regard to gravitational collapse (see Section 7.2).

5 FILAMENT IDENTIFICATION

The filament identification process first involves enhancement of elongated structures. We apply a new, PYTHON implementation of the multiscale Hessian-based ridge detection technique first described by Frangi et al. (1998). Ideally, the filament detection algorithm would be applied directly to the column density map. The filament analysis, however, requires large regions of continuous data to be successful otherwise artificial discontinuities may be perceived as filaments – a requirement that is not met here due to the 5σ intensity cutoff we enforce on the temperature (and ultimately column density) estimation. As a compromise, we apply the filament enhancement algorithm to the 850 μm intensity map.

The algorithm produces a 'ridgeness' map – the values of which represent the probability that a specific pixel is filamentary assuming the user-defined ridge enhancement parameters α, β and γ which give emphasis to elongation, prominence and scale, respectively (see Appendix A for an in-depth explanation of these parameters). In short, the β parameter defines the semimajor to semiminor axis ratio above which structure will be emphasized, while the γ parameter defines the structure emphasis according to scale. In this investigation, we set $\beta = 2$ and $\gamma = 1$, which defines filaments as structures with lengths at least double their widths and provides uniform response on all structure scales analysed, respectively. The α parameter adjusts the structure emphasis not according to geometry (as in β), but prominence. As a result, the value chosen for α depends upon the input data units and can be user-defined in order

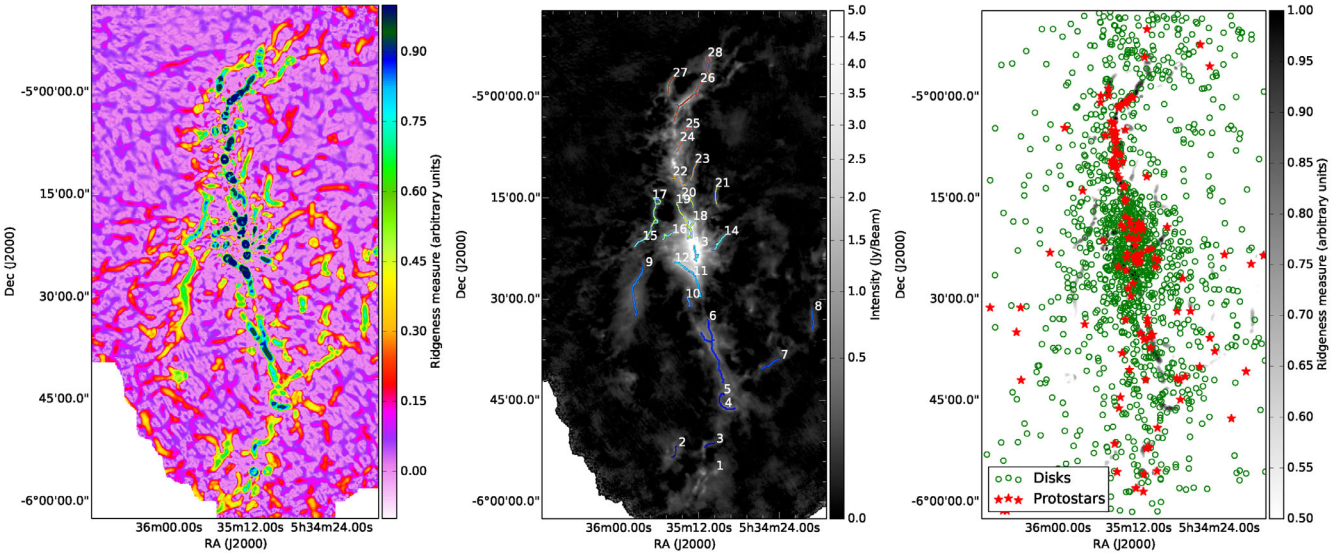

Figure 3. Left: filament enhanced 850 μm intensity map. Center: filament spine map overlaid on to a grey-scale 850 μm intensity map. Right: *Spitzer* source catalogue (Megeath et al. 2012) overlaid on to the grey-scale filament enhanced 850 μm intensity map – note the strong spatial correlation between filament spines and protostar positions.

to minimize the 'ridgeness' response of noise, while maximizing the response of true signal.

With the 'ridgeness' map generated, a threshold value related to the definition of a 'true' filament is defined. This value in effect controls the number of filaments detected in a map. If a low threshold is set, one delves into the lower probabilities of the 'ridgeness' map which will be dominated by noise-based structures in addition to the true astronomical filament signals. This value can be autodefined from the global statistics of the 'ridgeness' map, but in this instance we apply a user-defined value to reflect the filaments that would be intuitively identified by a human investigator. With the 'ridgeness' threshold applied, the binary image 'thinning' or skeletonization operation (Coelho 2013) is employed which produces single pixel width filament spines from the thresholded regions of high 'ridgeness'. The resulting filament spines serve as the centre point of the radial cross-sections and are displayed in Fig. 3 (centre). Finally, a standardized algorithmic separation technique (Coelho 2013) is applied to filter and partition the filament spines into distinct, isolated structures. All filaments containing less than 20 pixels (or filaments of length $\lesssim$0.25 pc) were discarded in this process. For further information regarding the filament identification process, please refer to the appendix.

6 FILAMENT RADIAL PROFILES

With the final set of separated filaments obtained, radial profiles are generated by extracting the column density and temperature values perpendicular to the filament spine. This extraction is achieved by applying a spatially smoothed Minimum Spanning Tree that connects points along the filament spine by linear functions, allowing for easy generation of perpendicular slices and determination of filament position angles. In particular, the Minimum Spanning Tree technique was selected due to its ability to trace a filament with bifurcation points, a property which could not be dealt with via polynomial fitting. Once the column density values are extracted along the filament bisector, a baseline is fitted to the far extents of the slice and removed to account for local background emission. Each slice is assessed based on the quality of baseline subtraction, the range of data values and the signal-to-noise ratio at the filament core. Once passed quality control, the individual slices are stored and the median values are derived in preparation for the fitting process. The median (as opposed to the average) is chosen in order to remove the biasing of the radial profile to that of bright point sources which are co-located with the filament. In addition to taking the median of the perpendicular slices, the column density values either side of the filament peak are also averaged, thus enforcing radial symmetry. The uncertainty estimates are generated by summing the individual slice uncertainty in quadrature and dividing by the square root of the number of samples that are contained within each bin.

In accordance with Arzoumanian et al. (2011) and for ease of parameter comparison, we select the Plummer-like profile (Nutter et al. 2008) as the idealized three-dimensional radial structure of the filament,

$$\rho(r) = \frac{\rho_{\rm c}}{\left[1 + (r/R_{\rm flat})^2\right]^{p/2}}, \tag{4}$$

where the variables $\rho_{\rm c}$, $R_{\rm flat}$ and p describe the three-dimensional space density, the extent of the flattened region at the filament core and the radial decay parameter, respectively. In order to fit the observed two-dimensional projection of the filament, two transforms must be carried out on the idealized Plummer-like profile. First, to account for the line-of-sight (LOS) projection, the well-established Abel-transform is calculated which requires the assumption of a radially symmetric three-dimensional density distribution. Secondly, (and in contrast to Arzoumanian et al. (2011)) the two-dimensional idealized projection must then be convolved with the relevant beam profile of the instrument $B_{\rm filter}(x)$ –

$$\Sigma_{\rm obs}(x) = A \frac{\rho_{\rm c} R_{\rm flat}}{\left[1 + (x/R_{\rm flat})^2\right]^{\frac{p-1}{2}}} * B_{\rm filter}(x), \tag{5}$$

where the variable r describes the three-dimensional radial coordinate, x describes the plane-of-sky coordinate we observe and $*$ denotes the convolution operator. The parameter $A = \sec i \int_{-\infty}^{\infty} (1 + u^2)^{-p/2} {\rm d}u$ is a constant factor (for $p > 1$) related to the inclination angle of the observed filament to the plane of sky, which is assumed here to be $i = 0$ (Arzoumanian et al. 2011).

Here, we assume that both the 450 and 850 μm beams take the form of a two component, normalized Gaussian model (main beam with broad secondary component) as described by Dempsey et al. (2013). To draw well-informed conclusions from the fit parameters, we employ the PYTHON-based Bayesian analysis package PYMC (Patil, Huard & Fonnesbeck 2010). A deterministic model was employed based on equation (5) with uniform priors for ρ_c, R_{flat} and p of (0–2.8) $\times$ 10^6 g cm^{-3}, 0–0.13 pc and 0–10, respectively. Filaments 13 and 19 required larger ρ_c priors due to their high observed column densities. Non-uniform priors could have been used due to the existence of decay parameter values derived from the studies of Arzoumanian et al. (2011). However, due to the small number of completed samples and the difference in filament identification technique, the uniform priors were deemed to be most appropriate. The posterior distribution is generated via Metropolis–Hastings steps and is sampled a total of 50 000 times with the first 5000 discarded as burn-in. It should also be noted that the fitting process was limited to column density measurements made within 0.1 pc of the filament spine. This distance (∼0.2 pc in total) ensures we are well within the theoretical robust signal recovery for Gaussian sources (Salji et al. 2015).

Initial analysis of the filament radial temperature profiles suggests that the filaments are approximately isothermal (see Fig. 4). Thus, in order to reduce the column density uncertainty and ultimately improve the constraint of the Plummer-profile fit, we assume a single temperature for each filament corresponding to the average temperature of the central 0.1 pc. This results in two independent column density estimates from the 450 and 850 μm intensity measurements (according to equation 1) with uncertainty proportional to the thermal noise of the bolometers only. The FCF uncertainty does not reflect point-to-point uncertainty but merely a scaling factor which will affect only the estimates of ρ_c.

7 RESULTS

7.1 Detected filaments

The filaments identified through the application of the Hessian-based algorithm are predominantly located near the central ridge with only a few outliers to both the south and west. By eye, one can observe that the high 'ridgeness' values shown in Fig. 3 (left) correlate well with 'real' filament locations including those with extremely low-intensity emission. The filament average position angles take on a variety of values with the majority lying approximately parallel to the central large-scale filament. Additionally, the standard deviation of position angles within a single filament never exceeds 75°, with an average of 45° (see Table 1) – such values can provide key comparisons for hydrodynamic simulations of star-forming filaments. It should be noted that circular condensations often lie along the filament ridges, leading to sudden drops in the 'ridgeness' value that in turn may produce circular artefacts at those locations, see Fig. 3 (centre), Filament 17.

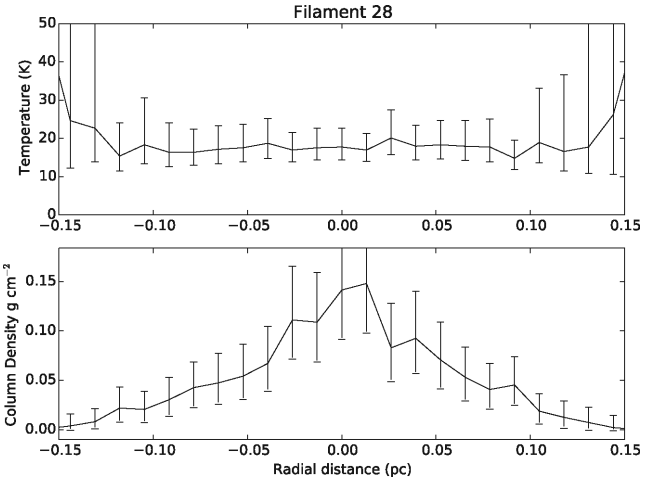

Figure 4. Median radial temperature and column density profiles of Filament 28 prior to making the assumption of isothermality and symmetrizing the profile. Note the large uncertainty that is propagated to the column density values which severely affects the ability to constrain the Plummer-profile parameters.

7.2 The gravitational stability of filaments

With the aid of the *Spitzer* source catalogue for Orion A North (Megeath et al. 2012), we can investigate the criticality of filaments with respect to gravitational collapse. We note that the mid-IR colour classification method employed in Megeath et al. (2012) leads to two-main categories of source – protostars (Class 0 or I) and discs (Class II). We make the assumption that if a Class 0/I protostar exists within 0.05 pc of a filament spine then it most likely originated from the filament which can be classed as supercritical to collapse. The distance of 0.05 pc was chosen as the radial extent of the filament core (see Fig. 5) and was used in the protostar/disc source counts as well as the total mass calculations. If one assumes the filament is a static, self-gravitating, isothermal cylindrical mass, the theoretical critical mass per unit length is given by $2c_s^2/G$ (Ostriker 1964) or equivalently $\sim 460 \langle \sigma_{vd} \rangle^2$ M$_\odot$ pc^{-1} where c_s is the isothermal sound speed $\sqrt{\frac{kT}{\mu m_H}}$ and the one-dimensional velocity dispersion is in units of km s^{-1}. This one-dimensional velocity dispersion can be extended to include non-thermal/turbulent support of the filament. The supporting velocity data described in Section 4 can be used to generate theoretical critical mass/length values from the equations given above. The σ_{vd} values obtained from the spectral line fitting were averaged over a region 0.05 pc from each of the filament spines and are included in Table 1 along with theoretical critical mass per unit lengths. By comparing the theoretical and measured mass per unit lengths, we can determine a 'criticality' parameter which indicates theoretically how far the observed filament is from gravitational equilibrium.

The additional measurements indicate that the majority of detected filaments are theoretically subcritical to collapse by factors as large as 10 despite the presence of young protostars in their immediate vicinity. However, the measurements of column density, temperature and velocity dispersion are consistent with other investigations of Orion A North (Buckle et al. 2012) to within factors of 2 or less. Thus, it is highly unlikely that the discrepancy between the presence of protostars and the theoretical criticality arises from the assumptions made to derive the quantities of mass, length and velocity dispersion. It is possible that localized regions along the filament may be supercritical to gravitational collapse while the filament remains globally subcritical. However, in regions where the presence of young protostars is strongly uncorrelated with the criticality, the discrepancy may result from inaccurate assumptions made concerning the Ostriker (1964) filament model.

Table 1. Radial profile fitting results for the 450 μm isothermal column densities. Filament 23 did not pass the automated radial profile filtering process primarily due to a poor signal-to-noise ratio at the filament core coupled with stronger emission from nearby filaments entering the radial bisector. All filament average position angles are measured East of North.'?' denotes the lack of information from supporting $C^{18}O$, $J = 3$–2 molecular line observations. The protostar and disc columns represent the total number of *Spitzer* sources within 0.05 pc of the filament spine. The criticality parameter is the ratio of measured mass/length to the theorized value $2\langle\sigma_{vd}\rangle^2/G$ (Ostriker 1964). A value >1 indicates that the kinetic energy of the gas should be unable to support against gravitational collapse.

Number	ρ_c (10^5 cm^{-3})	R_{flat} (pc)	p FWHM	Deconvolved (pc)	Mass/Length ($M_\odot$ pc^{-1})	Position Angle (°)	Protostars	Discs	$\langle\sigma_{vd}\rangle$ km s^{-1}	Theoretical critical Mass/Length ($M_\odot$ pc^{-1})	Criticality parameter
1	$1.6^{+0.3}_{-0.2}$	$0.090^{+0.011}_{-0.012}$	$7.74^{+1.38}_{-1.39}$	$0.086^{+0.024}_{-0.018}$	94±3	104.0±42.7	1	0	?	?	?
2	$0.8^{+0.1}_{-0.1}$	$0.117^{+0.010}_{-0.016}$	$6.76^{+1.01}_{-1.28}$	$0.122^{+0.031}_{-0.026}$	90±3	135.0±58.2	0	1	?	?	?
3	$2.0^{+0.7}_{-0.4}$	$0.054^{+0.012}_{-0.012}$	$4.08^{+0.98}_{-0.85}$	$0.081^{+0.041}_{-0.028}$	44±2	90.0±20.1	2	1	?	?	?
4	$2.6^{+0.4}_{-0.3}$	$0.073^{+0.008}_{-0.009}$	$7.00^{+1.18}_{-1.02}$	$0.074^{+0.018}_{-0.015}$	92±3	90.0±16.6	0	3	?	?	?
5	$0.5^{+0.1}_{-0.1}$	$0.089^{+0.017}_{-0.018}$	$7.06^{+2.03}_{-1.80}$	$0.090^{+0.042}_{-0.028}$	49±2	108.4±57.0	0	7	0.7	206±23	0.24±0.03
6	$2.9^{+0.5}_{-1.1}$	$0.029^{+0.015}_{-0.004}$	$2.32^{+0.61}_{-0.14}$	$0.079^{+0.052}_{-0.027}$	42±1	63.4±72.4	8	12	0.7	220±39	0.19±0.03
7	$1.5^{+1.0}_{-0.8}$	$0.048^{+0.047}_{-0.017}$	$3.18^{+3.43}_{-0.81}$	$0.091^{+0.161}_{-0.058}$	32±5	108.4±16.4	1	2	?	?	?
8	$1.1^{+0.6}_{-0.4}$	$0.073^{+0.036}_{-0.023}$	$4.32^{+2.74}_{-1.30}$	$0.104^{+0.111}_{-0.054}$	52±4	180.0±59.4	0	0	?	?	?
9	$0.7^{+0.2}_{-0.3}$	$0.055^{+0.047}_{-0.011}$	$2.57^{+1.96}_{-0.34}$	$0.131^{+0.162}_{-0.069}$	22±2	161.6±64.1	0	5	?	?	?
10	$0.7^{+0.1}_{-0.1}$	$0.074^{+0.006}_{-0.009}$	$8.80^{+0.88}_{-1.38}$	$0.065^{+0.013}_{-0.011}$	41±2	116.6±67.8	0	7	0.2	21±0	1.96±0.09
11	$1.1^{+2.2}_{-0.3}$	$0.092^{+0.034}_{-0.058}$	$4.10^{+2.03}_{-2.17}$	$0.138^{+0.246}_{-0.101}$	134±5	26.6±70.8	1	16	0.9	382±36	0.35±0.04
12	$3.6^{+1.8}_{-0.1}$	$0.096^{+0.001}_{-0.031}$	$9.74^{+0.21}_{-3.97}$	$0.080^{+0.033}_{-0.027}$	392±9	63.4±33.1	2	16	0.7	238±12	1.65±0.09
13	$227.7^{+31.2}_{-0.9}$	$0.044^{+0.000}_{-0.005}$	$3.77^{+0.01}_{-0.30}$	$0.070^{+0.005}_{-0.008}$	5300±190	161.6±62.7	5	14	1.3	834±6	6.35±0.23
14	$0.9^{+0.0}_{-0.0}$	$0.065^{+0.001}_{-0.001}$	$9.88^{+0.09}_{-0.19}$	$0.054^{+0.001}_{-0.002}$	30±1	135.0±25.0	1	8	1	431±45	0.07±0.01
15	$0.6^{+0.1}_{-0.1}$	$0.102^{+0.010}_{-0.014}$	$8.25^{+1.19}_{-1.52}$	$0.093^{+0.023}_{-0.019}$	32±7	135.0±19.9	0	0	0.4	75±2	0.42±0.09
16	$6.7^{+0.4}_{-0.4}$	$0.026^{+0.002}_{-0.001}$	$2.45^{+0.08}_{-0.06}$	$0.067^{+0.006}_{-0.006}$	88±3	116.6±37.3	1	5	0.9	355±23	0.25±0.02
17	$1.3^{+0.2}_{-0.2}$	$0.041^{+0.005}_{-0.005}$	$3.33^{+0.37}_{-0.30}$	$0.073^{+0.018}_{-0.015}$	19±6	146.3±51.0	0	7	0.6	146±11	0.13±0.04
18	$71.5^{+15.4}_{-0.6}$	$0.013^{+0.000}_{-0.002}$	$2.02^{+0.00}_{-0.08}$	$0.043^{+0.003}_{-0.006}$	252±9	135.0±52.7	5	21	0.7	229±2	1.10±0.04
19	$6.2^{+0.3}_{-0.1}$	$0.028^{+0.000}_{-0.001}$	$2.82^{+0.03}_{-0.07}$	$0.059^{+0.003}_{-0.003}$	76±4	45.0±53.9	3	13	0.8	301±27	0.25±0.03
20	$1.9^{+0.1}_{-0.0}$	$0.081^{+0.001}_{-0.002}$	$9.75^{+0.19}_{-0.43}$	$0.067^{+0.003}_{-0.002}$	48±2	63.4±61.5	2	17	0.6	177±3	0.27±0.01
21	$0.8^{+0.1}_{-0.0}$	$0.073^{+0.003}_{-0.004}$	$9.44^{+0.41}_{-0.82}$	$0.061^{+0.006}_{-0.005}$	34±9	161.6±72.0	0	2	?	?	?
22	$16.7^{+0.5}_{-0.7}$	$0.024^{+0.001}_{-0.001}$	$2.26^{+0.04}_{-0.03}$	$0.067^{+0.004}_{-0.003}$	105±4	45.0±38.2	2	7	0.5	138±2	0.76±0.03
24	$23.1^{+0.6}_{-1.5}$	$0.021^{+0.001}_{-0.000}$	$2.23^{+0.05}_{-0.02}$	$0.060^{+0.005}_{-0.003}$	238±8	161.6±9.3	3	6	0.6	163±1	1.46±0.05
25	$7.6^{+1.1}_{-0.9}$	$0.023^{+0.003}_{-0.002}$	$2.15^{+0.10}_{-0.09}$	$0.070^{+0.014}_{-0.012}$	74±3	71.6±46.2	1	0	0.8	315±6	0.23±0.01
26	$15.4^{+2.3}_{-0.5}$	$0.020^{+0.001}_{-0.002}$	$2.22^{+0.03}_{-0.09}$	$0.059^{+0.006}_{-0.008}$	125±3	135.0±34.2	11	8	0.6	142±1	0.88±0.02
27	$5.0^{+0.4}_{-0.4}$	$0.042^{+0.003}_{-0.003}$	$3.48^{+0.21}_{-0.17}$	$0.073^{+0.009}_{-0.008}$	87±9	161.6±15.1	2	3	0.5	116±1	0.75±0.08
28	$5.9^{+0.5}_{-0.5}$	$0.026^{+0.002}_{-0.002}$	$2.44^{+0.10}_{-0.08}$	$0.067^{+0.009}_{-0.008}$	48±1	135.0±69.1	1	3	?	?	?

7.3 The Plummer-profile parameters

Due to the assumption of isothermality discussed in Section 6, the 450 μm column density profile is generated at higher resolution but with poorer noise characteristics (due to atmospheric opacity variations) than the corresponding 850 μm profile. Results from the isothermal column density profile fitting demonstrate mild global constraint of the Plummer-profile parameters see Fig. 6.

The increased sampling and higher resolution of the 450 μm data provided posteriors in line with, but more strongly peaked than the 850 μm data, despite the lower sensitivity. As a result, only the 450 μm medians and 1σ standard deviations of the posterior distributions for the parameters in equation (5) are listed in Table 1. The filament core densities ρ_c (Fig. 6, bottom) demonstrate a wide range of values, with good agreement between the 450 and 850 μm posterior histograms, peaking∼0.5–1 × 10^5 cm^{-3}. Similarly, R_{flat} takes on a wide array of values, with most filaments characterized by flattened inner regions extending between 0.02 and 0.08 pc. While the parameters ρ_c and R_{flat} provide some useful quantities, the physical conditions that provide stability against gravitational collapse are predominantly represented through the radial decay parameter p. Since Ostriker's seminal paper on self-gravitating, isothermal, equilibrium cylinders ($p \approx 4$), multiple analytical cylindrical models including support mechanisms such as logatropic equations of state and magnetic fields have been derived (Fiege & Pudritz 2000). These theoretical models of filament structure predict a range of p values between 1 and 4. The posterior histogram of p values (Fig. 6, top) demonstrates that the majority of filaments exhibit $p = 1.5$–3, with a mode around $p = 2.2$ suggesting that the Ostriker (1964) model is not well represented in reality. While these values are consistent with previous investigations of filament structure (Arzoumanian et al. 2011), the spread of values in the radial decay parameter p makes it difficult to differentiate between many of the theoretical support mechanisms. This result is consistent with those of Juvela et al. (2012) who demonstrate that at a distance of 400 pc (with Herschel instruments), the errors in the parameters of the Plummer-profile are several tens of per cent. It should be noted that the rise in the p posterior for large values of p is likely caused by the dominance of bright point sources that are co-located with the

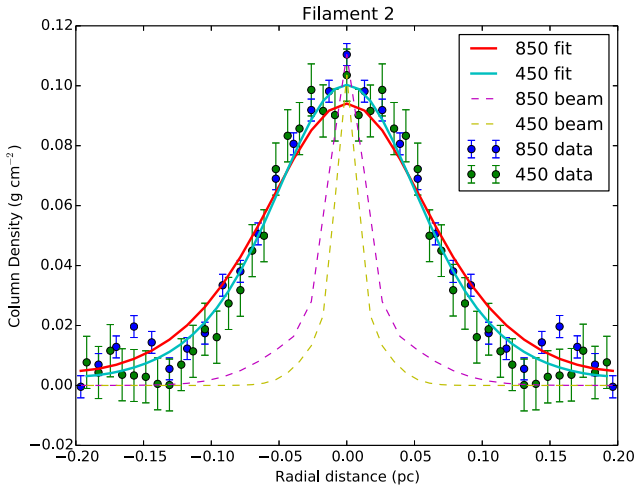

Figure 5. Median profile for Filament 2, the LOS Plummer-profile posterior median fit values are also plotted. Note that the filament is well-resolved at both 450 and 850 μm.

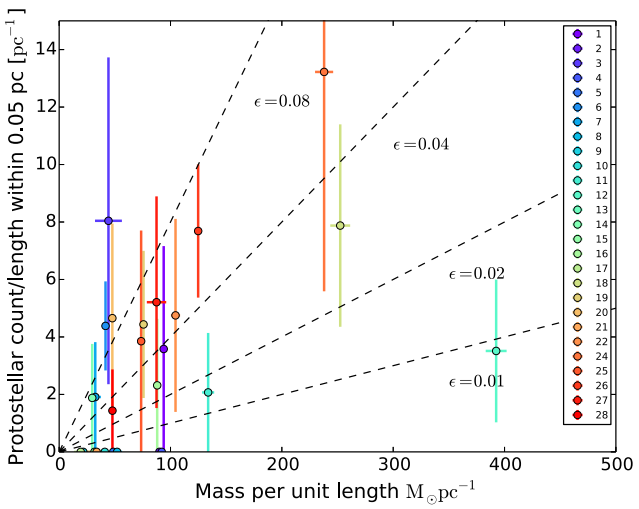

Figure 7. Measured mass/length plotted against protostellar source count/length within ∼0.05 pc. The dotted lines indicate the star formation efficiency – filaments with extremely large mass/lengths have been excluded for ease of viewing the majority of filaments. The vertical error bars are given according to Poisson counting uncertainty.

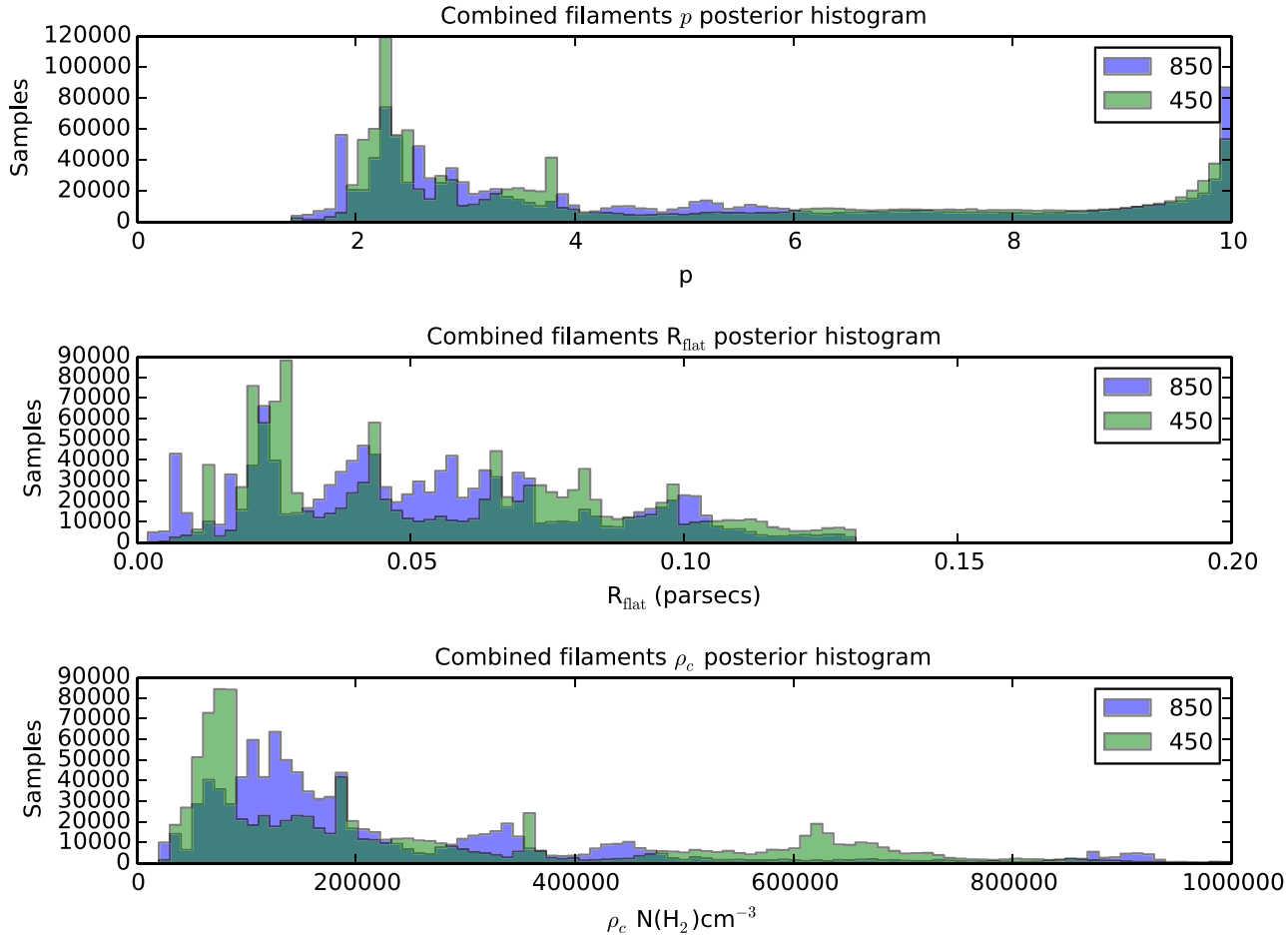

Figure 6. The combined Plummer-profile parameter posterior histograms for all filaments.

filament, resulting in a radial profile approaching that of the beam. As a result, the beam-convolved fitting process will yield anomalously high values of p.

7.4 Characteristic widths of filaments

The deconvolved best-fit parameters and their uncertainties were used to derive the deconvolved FWHM values and their corresponding uncertainty (see Table 1). It should be noted that these FWHM values do *not* correspond to a Gaussian FWHM as in Arzoumanian et al. (2011), but rather an FWHM in the general sense i.e. the width of a peaked function at half the value of its maximum. The average FWHM of the filaments observed is $0.08^{+0.07}_{-0.03}$ pc or 0.08 ± 0.02 pc if one simply considers the spread of measured widths. This value is consistent with those measured in Arzoumanian et al. (2011) and thus support the observation of characteristic filament widths of $\sim$0.1 pc. However, the beam-convolved fitting technique used in this investigation and the superior resolution of SCUBA-2 is likely to produce a more accurate representation of the true filament FWHM than the Gaussian quadrature subtraction of the beam profile used in Arzoumanian et al. (2011).

8 SPATIAL DISTRIBUTION OF FILAMENTS AND PROTOSTARS

In addition to the extraction of quantities such as the mass per unit length and radial decay parameters, the number of sources as a function of radial distance from the filament may be obtained, allowing for an investigation into the spatial correlation of different YSOs to their (postulated) parent filaments.

8.1 Episodic star formation

If one assumes that the majority of star formation occurs within high column density filaments, a much greater spatial correlation would be expected between filament and Class 0/I sources versus Class II sources. The observed respective Class durations are 10^4–10^5 and 10^6 yr (Larson 2003) allowing for much greater movement of the more evolved protostars from their parent filament. Previous radial velocity studies of protostars suggest a relative gas to source velocity of $\sim$1 km s^{-1} (Covey et al. 2006). Thus, we estimate movements of $\sim$0.05 and 1 pc for Class 0/I and Class II sources, respectively. In environments where the star formation process in the filament has ended, one may expect to see a steep increase in cumulative Class 0/I source count as function of distance from the parent filament, followed by a plateau. This plateau will be caused by the evolution of the Class 0/I source to a disc source during which it will migrate from its presumed birth site on the filament spine. Filament 26 displays this property, with a string of Class 0/I protostars lying due west of the filament suggesting large-scale eastward motion of the molecular gas with respect to the YSOs.

If an episodic star formation scenario is combined with an average relative gas to source velocity $\sim$1 km s^{-1} (Covey et al. 2006), then the period of time since the protostars were coincident with the filament spine may be derived – or equivalently (including previous assumptions), an age estimate. Fig. 8 shows the cumulative number of sources as a function of distance from Filament 26 – chosen due to its length and relative isolation. This plot shows the predicted rise and plateau of recently terminated star formation at $\sim 3.5 \times 10^4$ yr which lies in accordance with statistical source counting age estimates of the Class 0/I stage, assuming a weighted average of the Class 0/I duration (Larson 2003; Ward-Thompson et al. 2007b; Evans et al. 2009). It should be noted however, that the uncertainty on such values is rather difficult to calculate given that it relies on the filament spine position being accurate to within a few pixels. In addition, the average value of the gas to source velocity was not calculated specifically for the protostars used for this measurement and as such, inherits some degree of uncertainty.

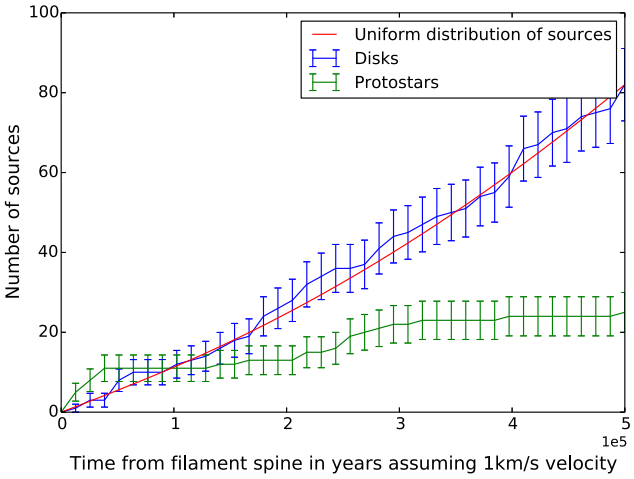

Figure 8. Cumulative number of *Spitzer* YSOs as a function of distance (translated to time – assuming a source to gas velocity dispersion of $\sim$1 km s^{-1}) from the filament spine. The errors shown are related to Poisson counting uncertainty. The red curve corresponds to a uniform distribution of sources in two-dimensions, implying that the cumulative number of disc sources is directly proportional to the area of measurement.

We also note that the uniform distribution of sources shown in Fig. 8 is *two-dimensional* as the red line is directly proportional to the source counting area which is centred on the filament spine. Thus, the distribution of disc sources, which is a three-dimensional quantity integrated along the LOS, appears to closely match that of a uniform plane. Since no function exists with radial symmetry that can be integrated along the LOS to produce a two-dimensional uniform distribution this suggests that there can be no radial symmetry in the distribution of disc sources around Filament 26. This result can be explained if the vast majority of disc sources near to Filament 26 were not formed there, but migrated there from distant filaments, thus relaxing the radial symmetry argument of the Abel transform. This explanation allows for the existence of a uniform distribution of sources in both two and three-dimensions, thus implying that star formation has only recently begun in Filament 26.

8.2 The star-forming efficiency of filaments

By combining the measured mass per unit length and the protostellar count per unit length, one may also examine the star formation efficiency of the filament as protostars per unit mass. This quantity translates directly to a star-forming efficiency determined over the last $\sim$50 000 yr (time taken to travel 0.05 pc at $\sim$1 km s^{-1}) if one assumes that each protostar extracts $\sim$1 M$_\odot$ from the filament – in accordance with mass function peak of previous studies (Nutter & Ward-Thompson 2007; Enoch et al. 2008; Salji et al. 2015). The results indicate a variety of efficiencies ranging between $\epsilon = 0.01$ and 0.1 for the filaments with protostars present (see Fig. 7).

Table 2. All quantities were derived by assuming a filament radius of 0.05 pc, a relative YSO to gas velocity dispersion of 1 km s^{-1} (Covey et al. 2006) and an average protostellar clump mass of 1 M$_\odot$.

Number	Mass (M$_\odot$)[a]	SFR (1×10^{-5} Protostars yr^{-1})[b] [c]	Mass Conversion 1×10^{-6} yr^{-1} [d]	Projected lifetime of filament (Myr)[e]
1	26.2	2	0.8	1.3
2	25.2	0	0	∞
3	11	4	3.6	0.3
4	26.5	0	0	∞
5	19	0	0	∞
6	76	16	2.1	0.5
7	17	2	1.2	0.8
8	17.7	0	0	∞
9	24.7	0	0	∞
10	9.5	0	0	∞
11	64.7	2	0.3	3.2
12	223.5	4	0.2	5.6
13	2196.9	10	0	22
14	15.8	2	1.3	0.8
15	9.7	0	0	∞
16	38	2	0.5	1.9
17	25.2	0	0	∞
18	160.3	10	0.6	1.6
19	51.2	6	1.2	0.9
20	20.5	4	1.9	0.5
21	11.1	0	0	∞
22	44	4	0.9	1.1
24	54	6	1.1	0.9
25	19.1	2	1	1
26	178.7	22	1.2	0.8
27	33.6	4	1.2	0.8
28	33.3	2	0.6	1.7

Notes. [a]Total filament mass contained within 0.05 pc of filament spine.
[b]Star formation rate – determined by counting the number of protostellar sources within 0.05 pc which at a relative YSO to gas velocity dispersion of 1 km s^{-1} corresponds to $\sim$50 000 yr.
[c]The total filament SFR corresponds to 1.04×10^{-3} M$_\odot$ yr^{-1} which lies in direct accordance with Hillenbrand (1997).
[d]This quantity is equivalent to SFR/Mass – assuming an average protostellar source mass of $\sim$1 M$_\odot$.
[e]Equivalent to Mass/SFR.

8.3 Projected lifetime of filaments

By summing the number of protostellar sources within 0.05 pc ($\sim$50 000 yr at 1 km s^{-1}) the star formation rate per filament (SFR$_i$) can be inferred (see Table 2). If we assume that the average pre-stellar core that becomes decoupled from the bulk motion of filament gas has a mass of $\sim$1 M$_\odot$, the relative filament mass that goes on to form stars per unit time may be derived. The inverse of this quantity yields the lifetime of filament i (assuming a constant SFR and no accretion on to the filament) i.e. $\frac{M_i}{\mathrm{SFR}_i}$ (where M_i denotes the total mass of the filament i). This calculation, on average yields a filament lifetime of $\sim$2.5 Myr for the Orion A North filaments. However, one can see that Filament 13 in particular has a much larger projected lifetime $\sim$20 Myr while the remainder lie around 1 Myr (see Table 2). This indicates that the population of short-lived filaments will quickly be drained of their mass without long-term accretion or a strongly varying SFR. In stark comparison to this, while Filament 13 contains over 60 per cent of the filamentary mass in the ISF, it accounts for less than 10 per cent of the current star formation in Orion A North resulting in a large projected lifetime. Previous estimates of molecular cloud lifetimes lie in accordance with the projected lifetime of Filament 13, $\sim$20 Myr (Larson 1994; Murray 2011). It should be noted however, that such filaments can be destroyed by a variety of processes such as stellar feedback and supernovae not only via loss of mass to the star formation process.

8.4 Cluster age estimation

If one assumes that all of the YSOs localized to the ISF were once formed in filaments, then dividing the the total number of YSOs (N_{YSO}) by the total SFR of all the filaments $\sum_{i=0}^{n} \mathrm{SFR}_i$ (where i denotes filament identifier and n is the total number of filaments) will yield an age estimate of the star formation process within the region.

$$t_{\mathrm{cluster}} = \frac{N_{\mathrm{YSO}}}{\sum_{i=0}^{n} \mathrm{SFR}_i}. \quad (6)$$

This result relies upon three assumptions.

(i) The majority of star formation occurs in filaments, a reasonable assumption given the spatial correlation of the filaments and Class 0/I protostars (André et al. 2010).

(ii) The SFR has remained relatively constant within the cluster. However, evidence suggests this second assumption is untrue and that the SFR in the Orion nebula Cluster has been increasing up until this point (Hillenbrand 1997; Murray 2011). To first order however, this is a reasonable approximation or at the very least provides a lower limit of the cluster age.

(iii) Once more assume that the relative velocity dispersion between the YSOs and molecular gas is $\sim$1 km s^{-1} (Covey et al. 2006).

(iv) Each protostar on average carries 1 M$_\odot$ of material (Nutter & Ward-Thompson 2007; Enoch et al. 2008; Salji et al. 2015).

Assuming all of the above, the resulting total, filament, SFR within the Orion ISF is 1×10^{-3} M$_\odot$ yr^{-1} which lies in exact accordance with previous estimates derived through isochrone fitting (Hillenbrand 1997). The result of equation (6) yields a cluster age estimate of 1.4 Myr – a value which once more lies in accordance with age estimates of the Orion nebula Cluster through alternate methods (Hillenbrand 1997; Peterson et al. 2008). Again, this age estimate is a lower limit if one assumes more realistically that the SFR has increased up until this point in time (Hillenbrand 1997).

8.5 An alternate view of filaments

A recent study by Gómez & Vázquez-Semadeni (2014) simulating molecular cloud formation from colliding flows suggests that the filaments we observe are far from static and are in fact long-lived features through which the gas flows into a central cluster. The filaments are long-lived because they accrete from their environment while simultaneously accreting on to the clumps within them; they are essentially the loci where flows change from accreting in two-dimensions to accreting in one-dimension (Gómez & Vázquez-Semadeni 2014). The filaments observed in Orion A North are consistent with this model given the following observations.

(i) There appears to be no correlation between the state of criticality according to the Ostriker (1964) filament model and the presence of protostars, which casts doubt upon the basic model assumptions of equilibrium and/or iso-thermality.

(ii) The measured projected lifetimes of filaments are very short relative to average molecular cloud lifetimes (Murray 2011; Larson 1994). Since similar filaments are observed in many other star-forming regions, it would suggest that these structures are relatively long-lived, implying that they are constantly accreting matter in order to maintain their presence. Alternatively, these filaments may themselves represent large-scale accretion flow structures on to the central OMC-1 clump.

(iii) Buckle et al. (2012) comment on the existence of a velocity gradient in the north–south direction of the ISF which may be consistent with a large-scale flow. However, this observation requires in-depth analysis of the filament velocity structure to verify this claim.

9 CONCLUSION

We successfully applied a new filament identification algorithm adapted from the work of Frangi et al. (1998) to a column density map of Orion A North derived from SCUBA-2 observations at 450 and 850 μm. We confirm that the deconvolved global filament parameters are mildly constrained with the simplified assumption of filament isothermality and plane of sky inclination. The majority of filaments exhibit radial decay parameters p between 1.5 and 3, which suggests that the Ostriker (1964), $p = 4$ filament model is inconsistent with observations. However, our results do not provide sufficient constraint to differentiate between most theoretical filament support mechanisms. It is possible that high-resolution and high-sensitivity follow-up investigations of multiple filaments with the Atacama Large Millimetre Array (ALMA) can overcome these barriers.

The results of the Plummer-profile fitting yield an average filament width of $0.08^{+0.07}_{-0.03}$ pc which lie in accordance with the observation of characteristic filament widths of ∼0.1 pc as suggested by Arzoumanian et al. (2011). Follow-up analysis of a wide range of star-forming molecular clouds is required to further confirm this property.

Using supporting velocity data in the form of HARP $C^{18}O$ $J = 3$–2 spectral maps, we deduce that the majority of theoretical critical filament mass per unit lengths are much larger than their observed values despite the presence of protostars in their immediate vicinity. This result further suggests departure from the isothermal, self-gravitating cylinder of Ostriker (1964) due to this apparent mismatch between the observed and theoretical gravitational criticality. With the aid of YSO classification and positional data obtained from *Spitzer* (Megeath et al. 2012) we deduce the following five results.

(i) The filaments in Orion A North display a variety of star-forming efficiencies ranging between $\epsilon = 0.01$ and 0.1.

(ii) The presence of young protostars is not correlated with the filament criticality parameter – casting doubt upon the model assumptions of equilibrium and/or isothermality.

(iii) There exists an inconsistency between the projected lifetime of the majority of filaments and the star-forming regions they exist in, suggesting long-term accretion on to the filaments or episodic star formation.

(iv) We derive a cluster age by dividing the total number of YSOs in the ISF region by the sum of filament-based SFRs over all filaments within the ISF, yielding a star-forming age ≥1.4 Myr which lies in accordance with previous estimates (Hillenbrand 1997).

(v) The filaments studied here are broadly consistent with those produced in the models of Gómez & Vázquez-Semadeni. These filaments are long-lived, one-dimensional accretion flows that stream on to a central clump (in this instance OMC-1) while producing critical clumps within their boundaries that lead to the formation of young stars. Follow-up filamentary analysis of space-velocity cubes of multiple star-forming regions are required to confirm the theories of collapsing filamentary flows.

ACKNOWLEDGEMENTS

The JCMT is operated by the Joint Astronomy Centre on behalf of the Science and Technology Facilities Council of the United Kingdom, the National Research Council of Canada, and (until 2013 March 31) the Netherlands Organisation for Scientific Research. Additional funds for the construction of SCUBA-2 were provided by the Canada Foundation for Innovation. This research used the facilities of the Canadian Astronomy Data Centre operated by the National Research Council of Canada with the support of the Canadian Space Agency.

REFERENCES

André P. et al., 2010, A&A, 518, L102
Arzoumanian D. et al., 2011, A&A, 529, L6
Buckle J. V. et al., 2012, MNRAS, 422, 521
Chapin E. L., Berry D. S., Gibb A. G., Jenness T., Scott D., Tilanus R. P. J., Economou F., Holland W. S., 2013, MNRAS, 430, 2545
Coelho L., 2013, J. Open Res. Softw., 1, e3
Covey K. R., Greene T. P., Doppmann G. W., Lada C. J., 2006, ApJ, 131, 512
Dempsey J. T. et al., 2013, MNRAS, 430, 2534
Enoch M. L., Evans N. J., II, Sargent A. I., Glenn J., Rosolowsky E., Myers P., 2008, ApJ, 684, 1240
Evans N. J., II et al., 2009, ApJS, 181, 321
Fiege J. D., Pudritz R. E., 2000, MNRAS, 311, 85
Frangi R. F., Niessen W. J., Vincken K. L., Viergever M. A., 1998, in Wells W. M., Colchester A., Delp S., eds, Lecture Notes in Computer Science, Vol. 1496, Medical Image Computing and Computer-Assisted Intervention - MICCAI'98. Springer-Verlag, Berlin, p. 130
Gómez G. C., Vázquez-Semadeni E., 2014, ApJ, 791, 124
Hill T. et al., 2011, A&A, 533, A94
Hillenbrand L. A., 1997, ApJ, 113, 1733
Holland W. S. et al., 2013, MNRAS, 430, 2513
Johnstone D., Bally J., 1999, ApJ, 510, L49
Juvela M., Malinen J., Lunttila T., 2012, A&A, 544, A141
Kackley R., Scott D., Chapin E., Friberg P., 2010, in Radziwill N. M., Bridger A., eds, Proc. SPIE Conf. Ser. Vol. 7740, Software and Cyberinfrastructure for Astronomy. SPIE, Bellingham, p. 77401Z
Larson R. B., 1994, in Wilson T. L., Johnston K. J., eds, Lecture Notes in Physics, Vol. 439, The Structure and Content of Molecular Clouds. Springer-Verlag, Berlin, p. 13
Larson R. B., 2003, Rep. Prog. Phys., 66, 1651
Li Z.-Y., Nakamura F., 2006, ApJ, 640, L187
Lombardi M., Alves J., Lada C. J., 2010, A&A, 519, L7
McKee C. F., Ostriker E. C., 2007, ARAA, 45, 565
Megeath S. T. et al., 2012, ApJ, 144, 192
Muench A., Getman K., Hillenbrand L., Preibisch T., 2008, Reipurth B., ed., ASP Monograph Publications, Vol. 4, Handbook of Star Forming Regions, Volume I: The Northern Sky. Astron. Soc. Pac., San Francisco, CA, p. 483
Murray N., 2011, ApJ, 729, 133
Nutter D., Ward-Thompson D., 2007, MNRAS, 374, 1413
Nutter D., Kirk J. M., Stamatellos D., Ward-Thompson D., 2008, MNRAS, 384, 755
Ostriker J., 1964, ApJ, 140, 1056
Patil A., Huard D., Fonnesbeck C. J., 2010, J. Stat. Softw., 35, 1
Peterson D. E. et al., 2008, ApJ, 685, 313
Pon A., Johnstone D., Heitsch F., 2011, ApJ, 740, 88

Salji C. J., Richer J. S., Buckle J. V., 2015, MNRAS
Schlafly E. F. et al., 2014, ApJ, 786, 29
Ward-Thompson D. et al., 2007a, PASP, 119, 855
Ward-Thompson D., André P., Crutcher R., Johnstone D., Onishi T., Wilson C., 2007b, Protostars and Planets V. Univ. Arizona Press, Tucson, AZ

APPENDIX A: HESSIAN-BASED RIDGE ENHANCEMENT

To discuss in depth the automated identification of morphological structure, one must first describe such structure mathematically. Within two-dimensional space, there are two distinct morphologies that exist, 'blobs' and 'ridges', though the definitions given here apply to a general, n-dimensional space in which there are n distinct morphologies. A 'blob' can be described as a portion of a smoothly varying function with a local maxima in ALL of the n-dimensions that contain $f(x_n)$, $x = \{x_1, x_2, \ldots, x_n\}$. Whereas, a 'ridge' or 'filament' can be described as a portion of a smoothly varying function with $n - 1$ local maxima in the n-dimensions that contain $f(x_n)$, $x = \{x_1, x_2, \ldots, x_n\}$

The simplest filament-like structures according to the definition given above are the lowest order functions that contain local maxima, i.e. those that have non-zero second-order derivatives and can be topographically described as ridge-like. Structures such as these are very common in all areas of science and as a result have been the focus of image processing research for many years. The basic process outlined below was originally designed for the enhancement of vessel structures in medical imaging (Frangi et al. 1998) – structures which show similarities to dusty star-forming filaments in molecular clouds. Consider now a small portion of an image $g(x, y)$. For small values of x and y from the centre of the portion, one may express the local features as a Maclaurin series (expanded around the point (0,0)) to second order. The subscripts indicate the directional derivative in the x or y directions.

$$g(x,y) \approx g(0,0) + x g_x(0,0) + y g_y(0,0) + \frac{1}{2}\left(x^2 g_{xx}(0,0) + 2xy g_{xy}(0,0) + y^2 g_{yy}(0,0)\right). \quad \text{(A1)}$$

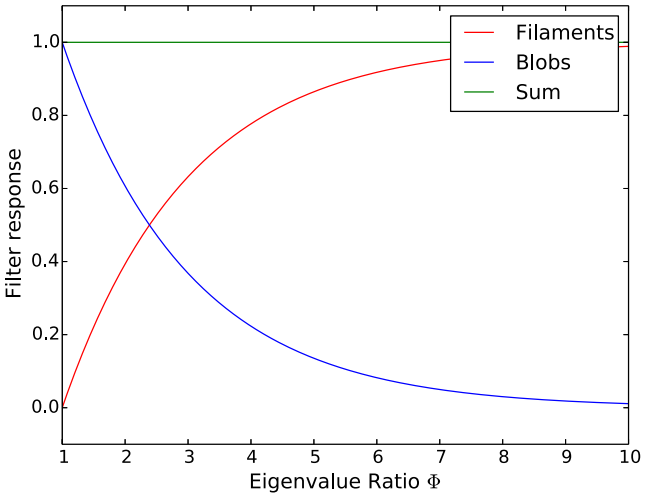

Figure A2. Illustration of the eigenvalue ratio filter. Note that the sum of the filter response functions is 1, which enforces a response from all objects.

Or in matrix form:

$$g(x,y) \approx \frac{1}{2}\begin{bmatrix} x & y \end{bmatrix}\begin{bmatrix} \frac{\partial^2 g(x,y)}{\partial x^2} & \frac{\partial^2 g(x,y)}{\partial x \partial y} \\ \frac{\partial^2 g(x,y)}{\partial y \partial x} & \frac{\partial^2 g(x,y)}{\partial y^2} \end{bmatrix}\begin{bmatrix} x \\ y \end{bmatrix} + \begin{bmatrix} x \\ y \end{bmatrix}\begin{bmatrix} \frac{\partial g(x,y)}{\partial x} & \frac{\partial g(x,y)}{\partial y} \end{bmatrix} + g(0,0), \quad \text{(A2)}$$

where

$$\mathbf{H} = \begin{pmatrix} \frac{\partial^2 g(x,y)}{\partial x^2} & \frac{\partial^2 g(x,y)}{\partial x \partial y} \\ \frac{\partial^2 g(x,y)}{\partial y \partial x} & \frac{\partial^2 g(x,y)}{\partial y^2} \end{pmatrix} \equiv \begin{pmatrix} \mathbf{H}_{xx} & \mathbf{H}_{xy} \\ \mathbf{H}_{yx} & \mathbf{H}_{yy} \end{pmatrix}. \quad \text{(A3)}$$

The matrix containing the second-order differentials is known as the Hessian, **H**. This matrix contains all the relevant information

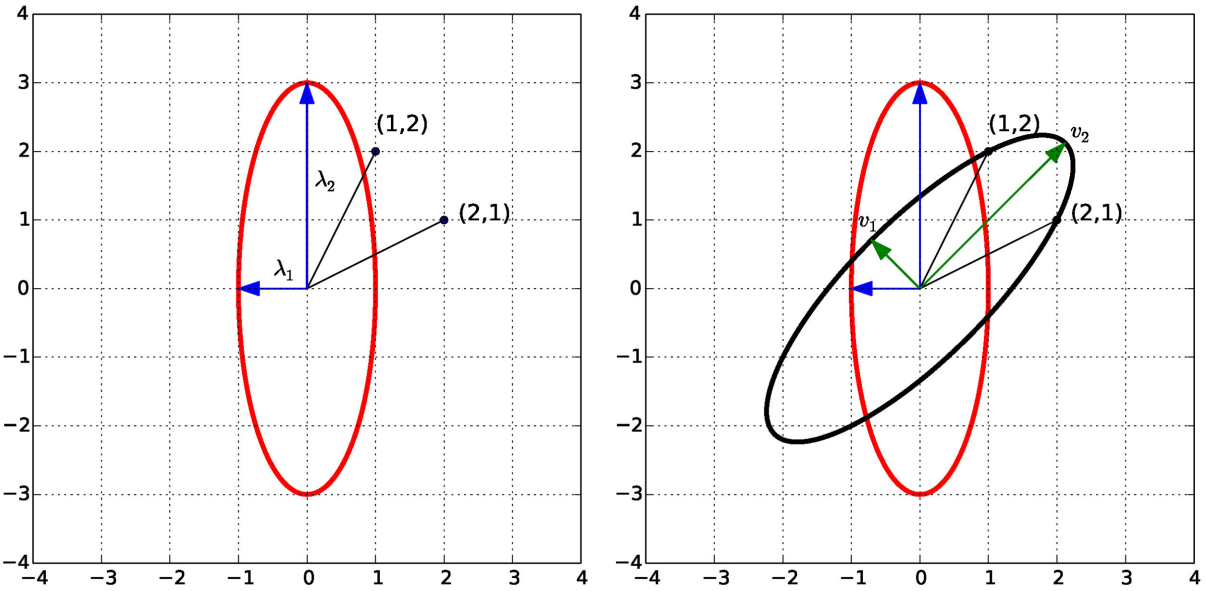

Figure A1. Left: elliptical projection of the eigenvalues of matrix **A**. Right: elliptical projection of the eigenvalues with semimajor axis rotated according to the eigenvector with largest corresponding eigenvalue.

concerning ridge-/filament-like structures and contains n^2 components for an n-dimensional space. The components may be approximated by convolving the image with the second-order derivatives of a Gaussian distribution $G(x, y)$ of a given scale σ in accordance with linear space theory which dictates that

$$\frac{\partial}{\partial x_i}(f * g) = \frac{\partial f}{\partial x_i} * g = f * \frac{\partial g}{\partial x_i}. \tag{A4}$$

Explicitly, for

$$G(x, y) = \frac{1}{\sqrt{2\pi\sigma^2}} \exp\left(-\frac{(x^2 + y^2)}{2\sigma^2}\right), \tag{A5}$$

then the Hessian components are calculated as follows,

$$\mathbf{H}_{xx} \approx \sigma^{\gamma}\left(g(x, y) * \frac{1}{\sigma^2}\left(\frac{x^2}{\sigma^2} - 1\right) G(x, y)\right) \tag{A6}$$

$$\mathbf{H}_{yy} \approx \sigma^{\gamma}\left(g(x, y) * \frac{1}{\sigma^2}\left(\frac{y^2}{\sigma^2} - 1\right) G(x, y)\right) \tag{A7}$$

$$\mathbf{H}_{xy} \equiv \mathbf{H}_{yx} \approx \sigma^{\gamma}\left(g(x, y) * \frac{xy}{\sigma^4} G(x, y)\right), \tag{A8}$$

where $*$ denotes the convolution operator.

In addition to the varying σ value, the value of γ can be varied to emphasize small or large-scale features with $\gamma = 1$ giving uniform enhancement across all scales. The images in Fig. A7 show the resulting components of the Hessian matrix after convolution with an 8 pixel σ scale parameter (this relatively large scale was chosen for easy viewing of the Hessian components). Once the Hessian components have been generated, the Hessian eigenvalues and eigenvectors may be analysed. The eigenvalues and eigenvectors of a two-dimensional matrix can be graphically represented as an ellipse with the semi-axes magnitudes given by the eigenvalues λ_1 and λ_2 (termed semiminor and semimajor, respectively) where $\lambda_2 \geq \lambda_1$, while the orientation given by the eigenvectors (see Fig. A1).

For example, matrix $\mathbf{A} = \begin{pmatrix} 1 & 2 \\ 2 & 1 \end{pmatrix}$ has resulting eigenvalues of $\lambda_1 = -1$ and $\lambda_2 = 3$ and the corresponding normalized eigenvectors $v_1 = \frac{1}{\sqrt{2}}\begin{pmatrix} -1 \\ 1 \end{pmatrix}$ and $v_2 = \frac{1}{\sqrt{2}}\begin{pmatrix} 1 \\ 1 \end{pmatrix}$. These are graphically represented in Fig. A1. It should now be clear that the eigenvalues of the Hessian matrix give the second-order derivative magnitude along the corresponding eigenvector axis and as such, the ratio of major (λ_2) to minor (λ_1) eigenvalues will be maximized for a filament like structure and minimized (tend towards unity) for a relatively circular object (henceforth 'blob-like'). With the knowledge of the eigenvalue sum ($\Sigma = |\lambda_2 + \lambda_1|$) and ratio ($\Phi = |\lambda_2/\lambda_1|$), all the information required to extract morphological features according to their elongation and prominence has now been acquired. Thus, this technique not only allows one to extract filamentary structure, but also *blob-like structure*.

The following three filters are applied to the information derived from the Hessian matrix:

(i) A hard-edged filter to select bright ($\lambda_2 < 0$) or dark ($\lambda_2 > 0$) features.

(ii) A soft-edged filter that selects features according to their eigenvalue ratio Φ. In this study, we use $1 - \exp(-(\Phi - 1)/\alpha)$ with an α value of 2 which means that all structures that are at least twice as long as they are wide are considered filaments. The $(\Phi - 1)$ accounts for the fact that the minimum ratio is 1 given that $\lambda_2 \geq \lambda_1$. To select blob-like features, one uses the soft-edged filter $\exp(-(\Phi - 1)/\alpha)$. This filter response (for both blobs and filaments) is shown in Fig. A2.

(iii) A soft-edged filter that selects prominent features according to their eigenvalue sum Σ. The filter takes the mathematical form of $1 - \exp(-\Sigma/\beta)$. The value of β can be chosen in a statistical or user-defined manner in order to eliminate noise structures. Thus 'prominent' features are essentially defined by the quantity β where structures with $\Sigma < \beta$ are considered to be noise.

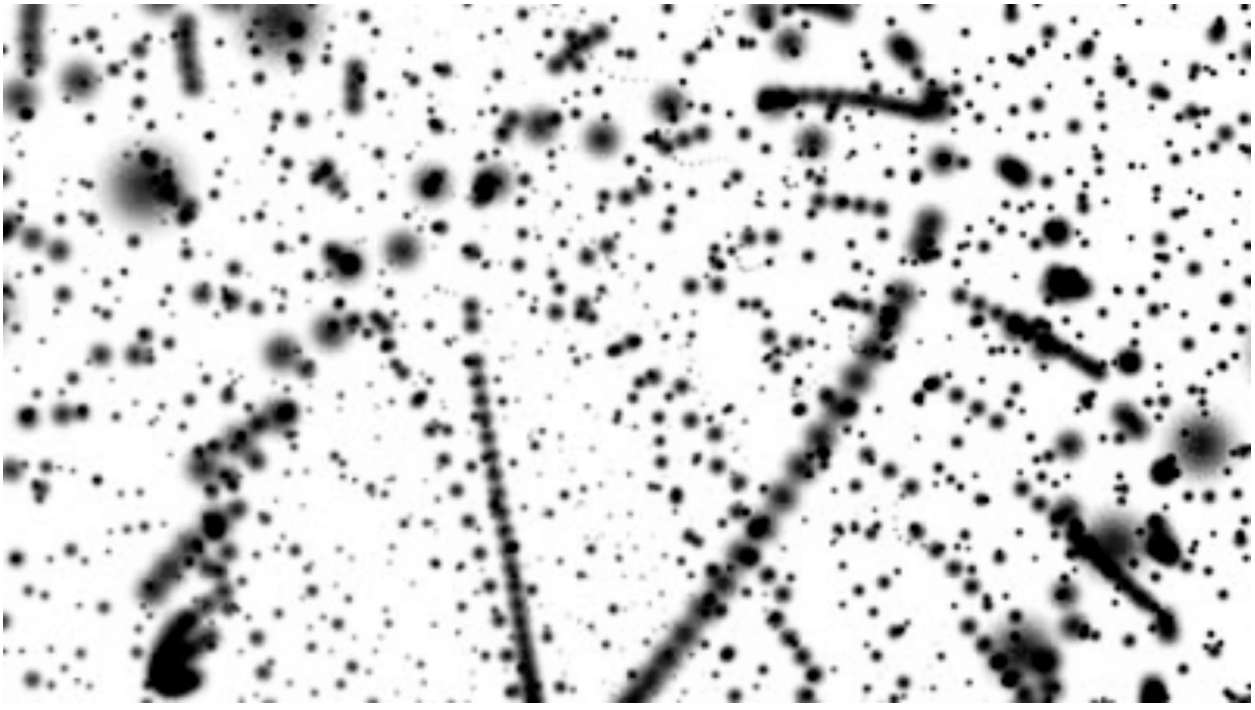

Figure A3. Example image to demonstrate the selection of structure according to its morphology.

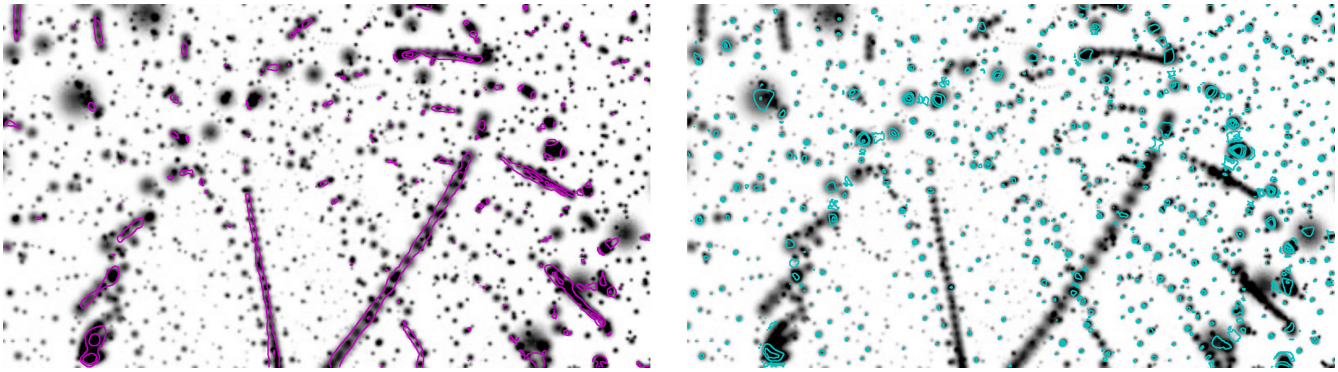

Figure A4. Left: magenta contours showing filament-like structure. Right: cyan contours showing blob-like structure. Both sets of contours range between 0.4 and 1.0 with increments of 0.1.

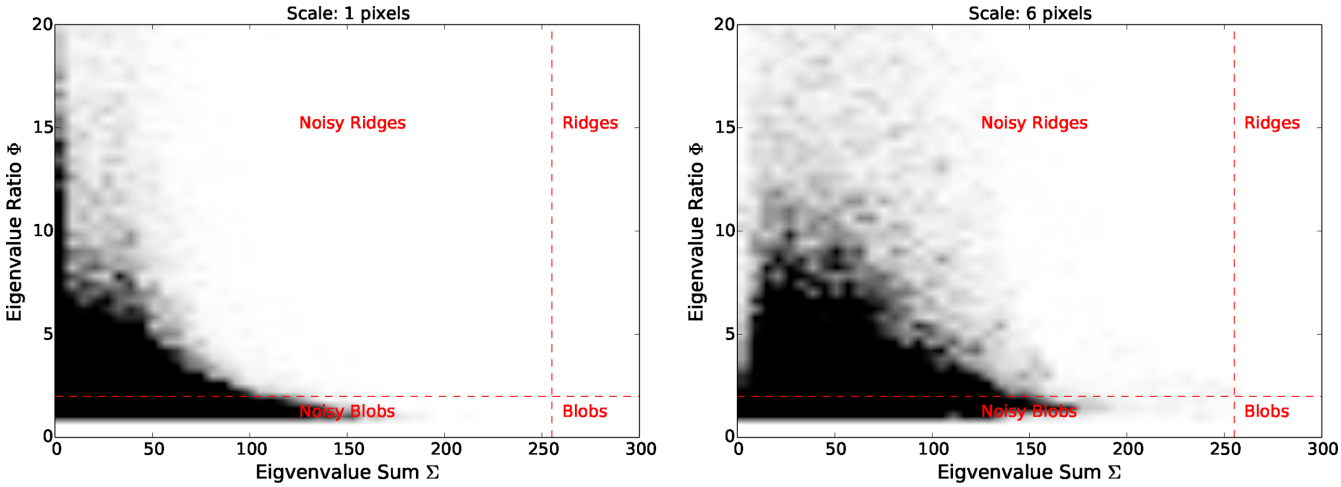

Figure A5. Two-dimensional histogram of eigenvalue sum Σ against eigenvalue ratio Φ at differing size scales. The red dotted lines show the locations of the soft filter edges thus splitting the morphology space into left: noise, right: real signal and top: filaments, bottom: blobs. The shift to the right as we move to larger scales indicates that features are more prominent on the larger scales.

Figure A6. Example image to test the filament enhancement method chosen primarily for the abundance of multiscale branch features.

The multiplication of these three filters will produce an image with the desired morphological structure enhanced for a given scale value σ. The morphological filter response for bright filamentary structure $\Lambda(x, y, \sigma)$ is therefore

$$\Lambda(x, y, \sigma) = \text{where}(\lambda_2(x, y, \sigma) < 0)(1 - \mathrm{e}^{-(\Phi(x,y,\sigma)-1)/\alpha}) \times (1 - \mathrm{e}^{-\Sigma(x,y,\sigma)/\beta}). \quad \text{(A9)}$$

The filtered images are produced for a given range of scale values to produce a stack of structure-enhanced images at different scales (see Fig. A8). To achieve a true multiscale enhancement of morphological structure, the peak filter response value is selected along the scale axis to be transferred to the final image while the scale at which the peak value is achieved is stored in an image that indicates the approximate scale of the structures identified. It should also be noted that knowledge of the Hessian eigenvalues alone allows one to determine the angle of the semimajor or minor axes of the projected ellipse which can be used to determine preferential filament orientations. Trivially, the eigenvector corresponding to the major eigenvalue also gives the directionality of elongation.

A1 Example 1 – blobs versus filaments

To illustrate the enhancement of structure according to its morphology, Fig. A3 shows an ideal example of the combination of both blob- and filament-like structure. Fig. A4 demonstrates the filtering according to morphology of Fig. A3. The scales for the filtering were between 1 and 10 pixels with an increment of 1 pixel. The soft-edged filters had turning point values at $\Phi = 2$ and $\Sigma = 200$ (the maximum value was 255 as the image was 8-bit). The morphology space may be examined in more detail by examining the two-dimensional histogram of eigenvalue sum Σ against eigenvalue ratio Φ (see Fig. A5). One can see from this figure how the array of eigenvalue ratios and sums varies with the scale parameter σ which

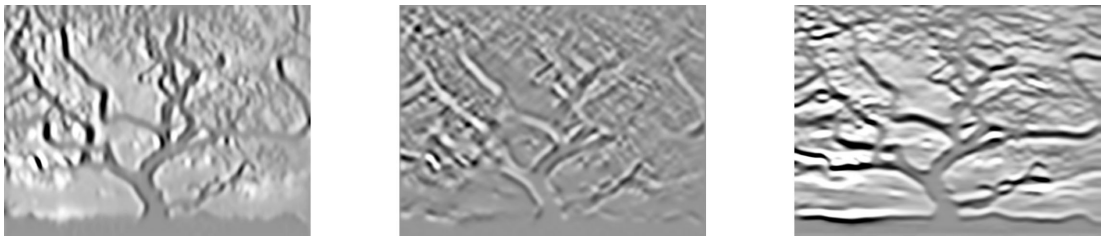

Figure A7. From left to right: $\mathbf{H}_{xx}$, $\mathbf{H}_{xy}$ and $\mathbf{H}_{yy}$ for $\sigma = 6$ pixels. Notice that $\mathbf{H}_{xx}$ and $\mathbf{H}_{yy}$ enhance the vertical and horizontal ridges, respectively, while the $\mathbf{H}_{xy}$ enhances the diagonal ridges.

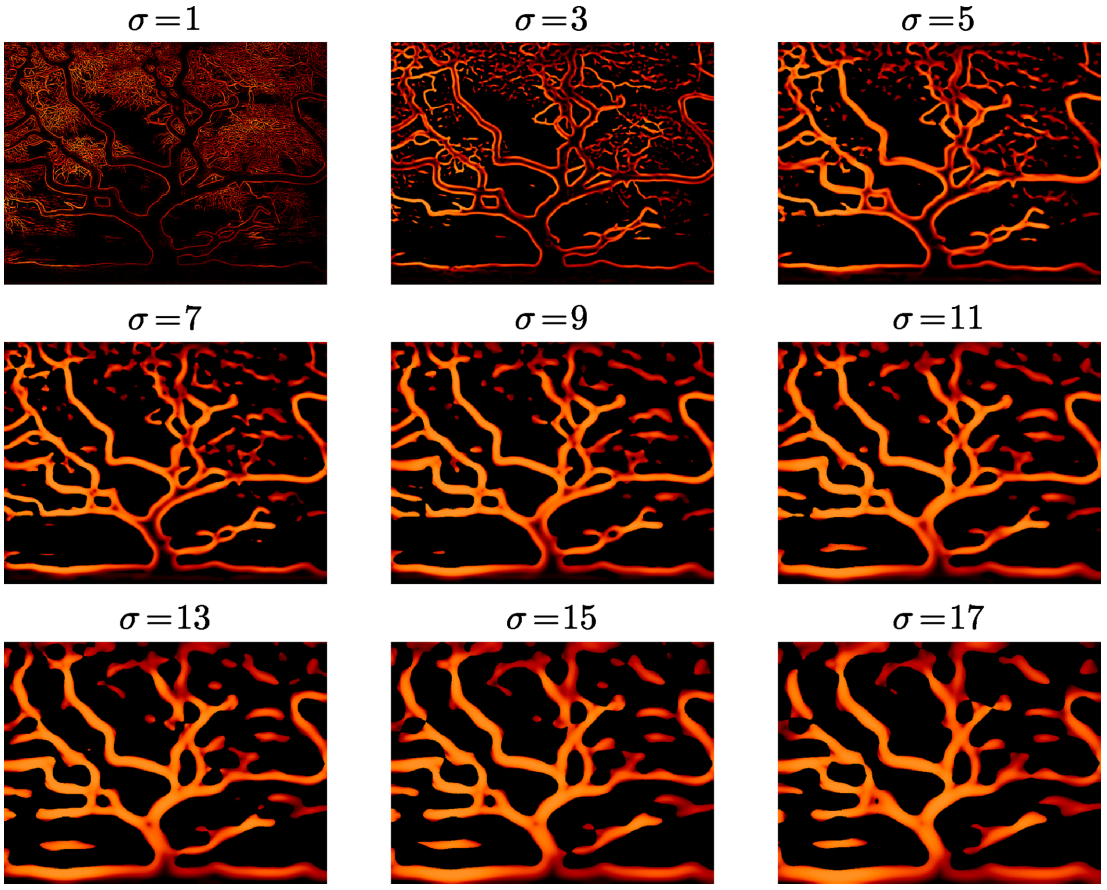

Figure A8. Filament enhanced images at different σ values – given in pixels.

indicates that large-scale features are more prominent in the image being analysed.

A2 Example 2 – multiscale enhancement

This second example focuses primarily on the multiscale nature of the morphological enhancement since many ridge detection algorithms suffer from the presupposition of a given filament scale, which is undesirable in this instance since the star-forming filament scale itself is a desired output. The image in Fig. A6 displays a great deal of filamentary structure spread over differing size scales to test the algorithm. It also provides an ideal opportunity for one to gain a more intuitive view of the Hessian components (see Fig. A7). Filamentary structure on all the scales specified by the range of σ values are enhanced, as shown in Fig. A9. It should be noted that while the examples shown in this work are all two-dimensional, this method of Hessian-based ridge detection generalizes easily to n-dimensional spaces. Follow-up work on three-dimensional space-velocity measurements of molecular clouds is currently in progress. The two-dimensional morphological structure enhancement PYTHON package described in this text will be made freely available in the near future.

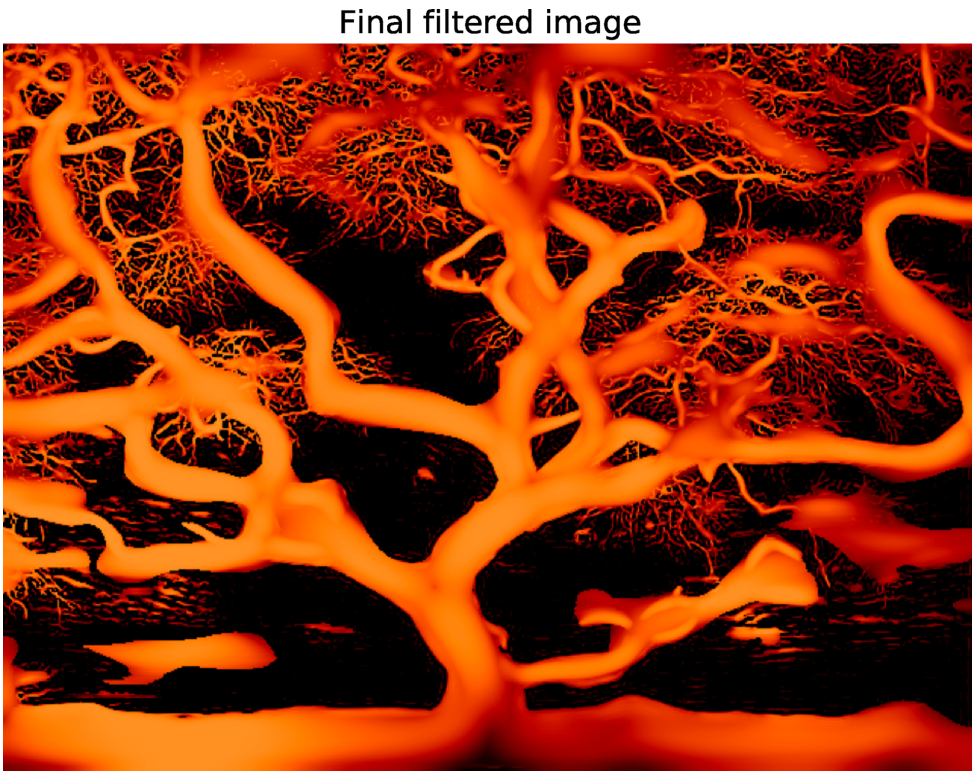

Figure A9. The final filament enhanced image, notice that filaments on all scales are represented in contrast to the scale dependent enhancement shown in Fig. A8.

This paper has been typeset from a TEX/LATEX file prepared by the author.